# Enhancement of interlayer exchange in an ultrathin 2D magnet

Dahlia R. Klein[1†], David MacNeill[1†], Qian Song[2], Daniel T. Larson[3], Shiang Fang[3], Mingyu Xu[4,5], R. A. Ribeiro[4,5,6], P. C. Canfield[4,5], Efthimios Kaxiras[3,7], Riccardo Comin[1], Pablo Jarillo-Herrero[1*]

[1]Department of Physics, Massachusetts Institute of Technology, Cambridge, MA 02139, USA
[2]Department of Materials Science & Engineering, Massachusetts Institute of Technology, Cambridge, MA 02139, USA
[3]Department of Physics, Harvard University, Cambridge, MA 02138, USA
[4]Ames Laboratory, U. S. Department of Energy, Iowa State University, Ames, IA 50011, USA
[5]Department of Physics and Astronomy, Iowa State University, Ames, IA 50011, USA
[6]Centro de Ciências Naturais e Humanas, Universidade Federal do ABC, Santo André, SP, Brazil
[7]John A. Paulson School of Engineering and Applied Sciences, Harvard University, Cambridge, MA 02138, USA

[†]These authors contributed equally to this work.
[*]Correspondence to: pjarillo@mit.edu

**Main Text:**

**Following the recent isolation of monolayer $CrI_3$[1], there has been a surge of new two-dimensional van der Waals magnetic materials[2-12], whose incorporation in van der Waals heterostructures offers a new platform for spintronics[5-9], proximity magnetism[13], and quantum spin liquids[14]. A primary question in this burgeoning field is how exfoliating crystals to the few-layer limit influences their magnetism. Studies on $CrI_3$ have shown a different magnetic ground state for ultrathin exfoliated films[1,5,6] but the origin is not yet understood. Here, we use electron tunneling through few-layer crystals of the layered antiferromagnetic insulator $CrCl_3$ to probe its magnetic order, finding a ten-fold enhancement in the interlayer exchange compared to bulk crystals. Moreover, temperature- and polarization-dependent Raman spectroscopy reveal that the crystallographic phase transition of bulk crystals does not occur in exfoliated films. This results in a different low temperature stacking order and, we hypothesize, increased interlayer exchange. Our study provides new insight into the connection between stacking order and interlayer interactions in novel two-dimensional magnets, which may be relevant for correlating stacking faults and mechanical deformations with the magnetic ground states of other more exotic layered magnets, such as $RuCl_3$[14].**

A key family of van der Waals magnets is the layered transition metal trihalides, which have been studied for decades as prototypical magnetic insulators[15,16] and as a platform for quasi-two-dimensional magnetism[17,18]. In the chromium trihalides, the Cr atoms are arranged in a honeycomb structure, with each Cr atom surrounded by six halide atoms in an octahedral geometry (Fig. 1a). The bulk crystals undergo a crystallographic phase transition from a monoclinic phase (space group $C2/m$) at room temperature to a rhombohedral phase (space group $R\bar{3}$) at low temperatures (below about 240 K for $CrCl_3$[19]). While the intralayer lattice spacings are largely

unaffected by this transition, the layer stacking sequence changes dramatically from rhombohedral ABC ordering at low temperatures to $AA_{1/3}$ stacking above 240 K, where each layer is displaced along the *a* axis by 1/3 of a lattice vector (Fig. 1a). Bulk $CrI_3$ and $CrBr_3$ are ferromagnetic below their Curie temperatures with moments aligned perpendicular to the *ab* plane; in contrast, bulk $CrCl_3$ is an antiferromagnet below its Néel temperature ($T_N$) of 14 K[19-21]. The Cr moments in each layer of $CrCl_3$ are ferromagnetically coupled, but couple antiferromagnetically across the van der Waals gap (Fig. 1b). However, this interlayer exchange coupling is weak and the magnetization of adjacent layers in bulk $CrCl_3$ can be aligned with a small in-plane magnetic field of about 0.2-0.25 Tesla[19,22].

The nature of stacking in few-layer chromium trihalides has recently garnered attention owing to the intriguing observation of an antiferromagnetic (AFM) ground state and interlayer exchange in few-layer $CrI_3$, in contrast to the ferromagnetic (FM) ground state of bulk crystals [1,3,5,6,23,24]. This crossover from FM to AFM interlayer coupling has led to theoretical investigations centered on the origin of the antiferromagnetic ground state in bilayer $CrI_3$[25-27]. First principles calculations predict that while the rhombohedral phase favors FM interlayer exchange, the monoclinic phase prefers an AFM alignment between the layers[27]. Thus, it is natural to propose that the observed AFM coupling results from a monoclinic stacking that persists to low temperatures in ultrathin $CrI_3$. However, this proposal has not been verified experimentally. For $CrCl_3$, both the crystal and magnetic structures of ultrathin films are unknown, and could provide valuable insight into how stacking order and exfoliation couple to interlayer interactions in these materials.

In this work, we use electron tunneling to probe the magnetic structure and interlayer exchange coupling of few-layer $CrCl_3$ crystals. We first use mechanical exfoliation to obtain crystallites ranging from two to four layers in thickness. We then fabricate vertical magnetic tunnel junctions using two few-layer graphite electrodes above and below each $CrCl_3$ flake and encapsulate with hexagonal boron nitride (Fig. 1c, see Methods). In the final step, each stack is transferred onto a silicon substrate with a 285 nm oxide layer and prepatterned Ti/Pd wires contacting the graphite electrodes. The junctions show a high resistance (Fig. 1d and Supplementary Materials) with a nonlinear current-voltage relationship characteristic of tunneling in the Fowler-Nordheim regime[28].

We find that the junction conductance increases dramatically when a magnetic field is applied in the plane of the crystal layers. Fig. 2a shows the differential conductance for a tetralayer device as a function of bias, at 300 mK and in-plane applied fields of 0 and 2 Tesla, where the AC excitation is 50 mV. The junction differential magnetoresistance

$$\mathrm{MR} = \frac{\frac{dI}{dV}(\mu_0 H_\parallel) - \frac{dI}{dV}(\mu_0 H_\parallel = 0)}{\frac{dI}{dV}(\mu_0 H_\parallel = 0)} \times 100\% \qquad (1)$$

is plotted in Fig. 2b, where $\mu_0 H_\parallel$ is 2 Tesla for the high-field measurement. We note that our definition of MR is mathematically equivalent to $(R_{LO} - R_{HI})/R_{HI}$, where $R_{HI}$ and $R_{LO}$ refer to resistances with and without an applied magnetic field, respectively. Consistent with previous results[6] and the theory of spin filter tunneling[29], the differential magnetoresistance peaks at a finite bias value near the onset of Fowler-Nordheim tunneling (between 625 and 875 mV). This peak corresponds to a maximum of spin-polarized tunneling when the applied bias is sufficient to allow efficient Fowler-Nordheim tunneling for majority-spin electrons, which experience a lower energy

barrier in the $CrCl_3$ when it is polarized, but not for minority-spin electrons, which experience a larger energy barrier. We further investigate the temperature and field dependence of this phenomenon by plotting the tunneling conductance of a $CrCl_3$ bilayer device as a function of both magnetic field and temperature (Fig. 2c). A vertical line cut of conductance versus temperature at zero applied field (Fig. 2d) shows a marked decrease in the conductance between 15 and 16 K. This drop reflects the onset of AFM alignment between the two layers in the junction, similar to the bulk $T_N$[19]. If the interlayer exchange were instead FM, one would expect increased conductance in the magnetic state due to the lowering of the energy barrier for majority-spin electrons[28].

In principle, there are two mechanisms that can provide magnetoresistance in our junctions: increasing the saturation magnetization *within* each layer (which decreases the majority-spin barrier[30]), and rotation of the magnetization in *adjacent* layers from antiparallel to parallel as the external field is increased (called the double spin filter effect[29,31]). We expect that the latter effect is dominant in our junctions because: i) the observed $T_N$ is similar to bulk crystals in which case the magnetization in each layer is nearly saturated at a value of 3 Bohr magnetons per Cr atom by 10 K, and ii) we observe only a single kink in the conductance versus magnetic field curves, rather than the two that would be expected for an alignment of the layers followed by a saturation of the intralayer magnetization.

To analyze our conductance versus applied magnetic field data at 4.2 K and to extract the interlayer exchange, we model the magnetization as fully saturated within each layer and coupled between layers via an AFM exchange field $H_E$ (see Supplementary Materials for the precise definition of our model and interlayer exchange field). The experimental magnetoresistance curves are shown in Fig. 3a. Consistent with the spin filter effect when tunneling through a magnetic insulating barrier[31,32], the magnetoresistance increases with barrier thickness from 9% in a bilayer $CrCl_3$ device up to 208% in a tetralayer $CrCl_3$ device (Fig. 3c). The normalized magnetoresistance curves are displayed in Fig. 3b to emphasize the difference in saturation fields. Surprisingly, in all devices, the AFM to FM transition occurs at a much higher field than for bulk crystals (roughly 0.2-0.25 Tesla[19,22]). These AFM-FM transition fields range from 0.85 Tesla in the bilayer junction to 1.65 Tesla in the tetralayer junction. The reported bulk interlayer exchange field is 0.084 Tesla[17]. However, based on the saturation fields in Fig. 3a, we calculate increased values for the exchange coupling of 0.86 Tesla, 0.96 Tesla, and 0.97 Tesla in bilayer, trilayer, and tetralayer $CrCl_3$, respectively (see Supplementary Materials for calculation of the interlayer exchange from the experimentally observed metamagnetic transition). The consistency of the extracted interlayer exchange coupling for different thicknesses, despite large differences in the saturation field, strongly supports our hypothesis that the magnetoresistance arises from alignment of magnetic moments in adjacent layers. These magnetoresistances thus demonstrate more than a ten-fold increase in the interlayer exchange strength when $CrCl_3$ is cleaved to the few-layer limit. Furthermore, the thickness dependence of the interlayer exchange in the few-layer films is weak and the interlayer exchange is seen to slightly *increase* with thickness in our devices. This suggests that the dramatic enhancement is due to a qualitatively different property of the exfoliated films compared to bulk (*i.e.* their stacking order).

In order to explore our hypothesis of stacking order as the origin of enhanced interlayer exchange, we performed Raman spectroscopy on both bulk and exfoliated thin $CrCl_3$ crystals (Fig. 4). The experiments were performed in a backscattering geometry with a 532 nm laser incident perpendicular to the crystal *ab* plane. The incident light was linearly polarized and inelastically-scattered photons were detected in the parallel-polarized channel (XX). The 247 $cm^{-1}$ Raman mode

of bulk $CrCl_3$ undergoes a marked peak shift close to 2 $cm^{-1}$ at the crystallographic phase transition near 240 K[33]. This excitation corresponds to out-of-plane vibrations of Cl atoms in the *ab* plane, which depend sensitively on the shearing of layers with respect to one another. To calibrate the peak position, we also fit the 209 $cm^{-1}$ Raman mode, which does not shift at the phase transition, and plot the difference between the two peak energies. We first studied the evolution of this energy difference upon cooling of a bulk crystal (Fig. 4a). Consistent with previous work[33], we observe a sharp shift in the peak energy difference between 240 and 250 K (see Supplementary Materials for complete spectra). Next, we examined the same peaks in an exfoliated crystal (35 nm thick) on a $SiO_2$/Si substrate. The peak difference shows minimal temperature dependence and no evidence of a transition even down to 10 K (Fig. 4b). We find similar results in an even thinner (8 nm thick) exfoliated crystal, with no apparent phase transition down to 180 K (Fig. 4c). This absence of a peak shift suggests that thin exfoliated $CrCl_3$ crystals remain in the high temperature monoclinic phase at low temperatures. Another explanation is that deformation of the crystal during the aggressive exfoliation process introduces stacking faults. In fact, repeated deformation of a bulk $\alpha$-$RuCl_3$ crystal by bending back and forth gives rise to stacking faults leading to a change in $T_N$[34]. Thus, the exfoliation process itself likely plays a role in modifying the physical properties of thin van der Waals crystals compared to their original bulk structures.

To further study the crystal phases of exfoliated versus bulk $CrCl_3$, we analyzed the energy of the 247 $cm^{-1}$ Raman peak as a function of polarization angle. In the rhombohedral $R\bar{3}$ phase this peak is produced by a doubly-degenerate $E_g$ mode, whereas in the monoclinic $C2/m$ phase it arises from a combination of closely spaced $A_g$ and $B_g$ modes[35,36]. In both cases, the two modes contributing to the observed peak have opposite polarization dependence. When they are degenerate, the opposite polarization dependences of these modes cancel out, leading to a single peak with constant intensity at one energy, as seen in the $R\bar{3}$ phase. But when the two modes are slightly offset in energy, their out-of-phase intensity variations lead to the observation of a combined peak whose peak position displays a fourfold modulation as a function of polarization angle (see Supplementary Materials for a detailed analysis). Based on these symmetry arguments, we can determine the crystal structure of bulk and thin films via polarized Raman spectroscopy. For a bulk crystal at 300 K (and therefore in the $C2/m$ phase), we observe a fourfold variation in the energy of this peak as we sweep the polarization angle (Fig. 4d). However, upon cooling the bulk sample to 80 K, the peak energy oscillations become an order of magnitude smaller. This change is indicative of the crystallographic phase transition to the $R\bar{3}$ phase by 80 K (the small, resolution-limited residual signal may arise from some regions pinned in the high-temperature structure, see Ref. 20). In contrast, we found that a thin (17 nm thick) exfoliated flake on a $SiO_2$/Si substrate has strong fourfold variation in the 247 $cm^{-1}$ mode peak position at both 300 K and 80 K (Fig. 4e). This result gives strong additional evidence that exfoliated $CrCl_3$ is in the monoclinic phase even at lower temperatures.

We note that the oscillation of the 247 $cm^{-1}$ Raman peak energy in the exfoliated crystal is somewhat smaller at 80 K than 300 K. This could arise from either a partial transition of the crystal into the low temperature phase, or some inherent temperature dependence of the peak oscillation due to inhomogeneous hardening of the closely-lying phonon lines. We cannot rule out either scenario, but expect that our junctions are uniformly in the monoclinic stacking order. This is because we only observe a single kink in the magnetoresistance versus field traces, ruling out the presence of a highly nonuniform interlayer exchange coupling. In one trilayer device (see Supplementary Materials) we did see a sharp increase in the magnetoresistance saturating around

0.15 Tesla, which could arise from a stacking fault within the barrier creating coexisting regions of monoclinic and rhombohedral stacking.

To understand the dependence of the interlayer exchange on the stacking type, we carried out density functional theory (DFT) calculations of the energy difference between the FM and AFM states for bilayer $CrCl_3$ with various stacking arrangements (see Supplementary Materials). We find that the $C2/m$-type stacking in the bilayer strongly favors an AFM interlayer alignment whereas the $R\bar{3}$-type phase can favor AFM or FM coupling, depending on the chosen DFT functional and interlayer spacing. Furthermore, the *difference* in interlayer exchange energy between the $C2/m$-type and $R\bar{3}$-type structures is relatively insensitive to the DFT functional used, and shows that the $C2/m$-type phase always has significantly larger AFM coupling than the $R\bar{3}$-type phase. For a realistic range of interlayer spacings from 0.55 nm to 0.65 nm, the calculated value of the interlayer exchange difference is on the same order as our experimental estimate. Overall, our calculations show that the $C2/m$-type phase has stronger AFM interlayer coupling than the $R\bar{3}$-type phase, consistent with the observed giant enhancement of interlayer exchange in ultrathin $C2/m$ $CrCl_3$.

In summary we have demonstrated a ten-fold increase in the interlayer exchange of ultrathin $CrCl_3$ crystals. We attribute this dramatic enhancement to the monoclinic low temperature crystal structure of exfoliated crystals. It is currently unknown if this stacking structure is the lowest energy configuration or is a metastable state pinned by disorder introduced by the exfoliation process. The low temperature monoclinic order even in very thick exfoliated crystals suggests that the latter explanation is correct. This result has important implications for understanding the unexpected magnetic behavior in the ultrathin chromium trihalides. For example, the FM to AFM transition observed in ultrathin $CrI_3$ is likely also a result of $C2/m$ stacking in the few-layer crystals, as has been predicted from first principles calculations[27]. We have also noticed a small increase in $T_N$ in our devices compared to the bulk. It is important to see if $T_N$ can be correlated with spatially resolved changes, such as stacking faults, using electron microscopy or second harmonic generation spectroscopy. Finally, our study opens the possibility to modify exchange couplings in other van der Waals magnets through strain, twisting, and other methods[42].

**References:**


1. Huang, B. *et al.* Layer-dependent ferromagnetism in a van der Waals crystal down to the monolayer limit. *Nature* **546,** 270–273 (2017).
2. Gong, C. *et al.* Discovery of intrinsic ferromagnetism in two-dimensional van der Waals crystals. *Nature* **546**, 265-269 (2017).
3. Huang, B. *et al.* Electrical control of 2D magnetism in bilayer $CrI_3$. *Nat. Nanotechnol.* **13**, 544-548 (2018).
4. Seyler, K. L. *et al.* Ligand-field helical luminescence in a 2D ferromagnetic insulator. *Nat. Phys.* **14,** 277–281 (2018).
5. Klein, D. R. *et al*. Probing magnetism in 2D van der Waals crystalline insulators via electron tunneling. *Science* **360**, 1218-1222 (2018).
6. Song, T. *et al.* Giant tunneling magnetoresistance in spin-filter van der Waals heterostructures. *Science* **360**, 1214-1218 (2018).
7. Wang, Z. *et al.* Very large tunneling magnetoresistance in layered magnetic semiconductor $CrI_3$. *Nat. Commun.* **9**, 2516 (2018).
8. Kim, H. H. *et al.* One million percent tunnel magnetoresistance in a magnetic van der Waals heterostructure. *Nano Lett.* **18**, 4885-4890 (2018).
9. Ghazaryan, D. *et al.* Magnon-assisted tunneling in van der Waals heterostructures based on $CrBr_3$. *Nat. Electron.* **1**, 344-349 (2018).
10. Kuo, C.-T. *et al.* Exfoliation and Raman spectroscopic fingerprint of few-layer $NiPS_3$ van der Waals crystals. *Sci. Rep.* **6**, 20904 (2016).
11. Lee, J.-U. *et al.* Ising-type magnetic ordering in atomically thin $FePS_3$. *Nano Lett.* **16**, 7433-7438 (2016).
12. Burch, K. S., Mandrus, D., and Park, J.-G. Magnetism in two-dimensional van der Waals materials. *Nature* **563**, 47-52 (2018).
13. Zhong, D. *et al.* Van der Waals engineering of ferromagnetic semiconductor heterostructures for spin and valleytronics. *Sci. Adv.* **3**, e1603113 (2017).
14. Banerjee, A. *et al.* Proximate Kitaev quantum spin liquid behavior in a honeycomb magnet. *Nat. Mater.* **15**, 733-740 (2016).
15. Dillon, J. F. and Olson, C. E. Magnetization, resonance, and optical properties of the ferromagnet $CrI_3$. *J. Appl. Phys.* **36**, 1259-1260 (1965).
16. Cable, J. W. *et al.* Neutron diffraction investigation of antiferromagnetism in $CrCl_3$. *J. Phys. Chem. Solids* **19**, 29-34 (1961).
17. Narath, A. and Davis, H. L. Spin-wave analysis of the sublattice magnetization behavior of antiferromagnetic and ferromagnetic $CrCl_3$. *Phys. Rev.* **137**, A163-A178 (1965).
18. Kuhlow, B. Magnetic ordering in $CrCl_3$ at the phase transition. *phys. stat. sol. (a)* **72**, 161 (1982).
19. McGuire, M. A. *et al.* Magnetic behavior and spin-lattice coupling in cleavable van der Waals layered $CrCl_3$ crystals. *Phys. Rev. Mater.* **1**, 014001 (2017).
20. McGuire, M. A., Dixit, H., Cooper, V. R. & Sales, B. C. Coupling of crystal structure and magnetism in the layered, ferromagnetic insulator $CrI_3$. *Chem. Mater.* **27,** 612–620 (2015).
21. McGuire, M. A. Crystal and magnetic structures in layered, transition metal dihalides and trihalides. *Crystals* **7**, 121 (2017).
22. MacNeill, D. *et al*. Gigahertz frequency antiferromagnetic resonance and strong magnon-magnon coupling in the layered crystal $CrCl_3$. Preprint available at https://arxiv.org/abs/1902.05669 (2019).

23. Jiang, S. *et al.* Controlling magnetism in 2D $CrI_3$ by electrostatic doping. *Nat. Nanotechnol.* **13**, 549-553 (2018).
*24*. Thiel, L. *et al.* Probing magnetism in 2D materials at the nanoscale with single spin microscopy. *Science* **364**, 973-976 (2019).
*25*. Jiang, P. *et al*. Stacking tunable interlayer magnetism in bilayer $CrI_3$. *Phys. Rev. B* **99**, 144401 (2019).
26. Soriano, D. *et al.* Interplay between interlayer exchange and stacking in $CrI_3$ bilayers. *Solid State Commun.* **299**, 113662 (2019).
27. Sivadas, N. *et al.* Stacking-dependent magnetism in bilayer $CrI_3$. *Nano Lett.* **18**, 7658-7664 (2018).
28. Simmons, J. G. Generalized formula for the electric tunnel effect between similar electrodes separated by a thin insulating film. *J. Apply. Phys.* **34**, 1793-1803 (1963).
29. Miao, G.-X., Müller, M., and Moodera, J. S. Magnetoresistance in double spin filter tunnel junctions with nonmagnetic electrodes and its unconventional bias dependence. *Phys. Rev. Lett*. **102**, 076601 (2009).
30. Moodera, J. S., Meservey, R., and Hao, X. Variation of the electron-spin polarization in EuSe tunnel junctions from zero to near 100% in a magnetic field. *Phys. Rev. Lett.* **70**, 853-856 (1993).
31. Worledge, D. C. and Geballe, T. H. Magnetoresistive double spin filter tunnel junction. *J. Appl. Phys.* **88**, 5277-5279 (2000).
32. Hao, X., Moodera, J. S., and Meservey, R. Spin-filter effect of ferromagnetic europium sulfide tunnel barriers. *Phys. Rev. B* **42**, 8235 (1990).
33. Glamazda, A. *et al.* Relation between Kitaev magnetism and structure in $\alpha$-$RuCl_3$. *Phys. Rev. B* **95**, 174429 (2017).
34. Cao, H. B. *et al.* Low-temperature crystal and magnetic structure of $\alpha$-$RuCl_3$. *Phys. Rev. B* **93**, 134423 (2016).
35. Bermudez, V. M. Unit-cell vibrational spectra of chromium trichloride and chromium tribromide. *Solid State Commun.* **19**, 693-697 (1976).
36. Larson, D. T. and Kaxiras, E. Raman spectrum of $CrI_3$: An *ab initio* study. *Phys. Rev. B* **98**, 085406 (2018).
37. Cao, Y. *et al.* Unconventional superconductivity in magic-angle graphene superlattices. *Nature* **556**, 43-50 (2018).

**Methods-Only References:**

38. Blöchl, P. E. Projector augmented-wave method. *Phys. Rev. B* **50**, 17953 (1994).
39. Kresse, G. and Furthmüller, J. Efficient iterative schemes for *ab initio* total-energy calculations using a plane-wave basis set. *Phys. Rev. B.* **54**, 11169 (1996).
40. Kresse, G. and Furthmüller, J. Efficiency of ab-initio total energy calculations for metals and semiconductors using a plane-wave basis set. *Comput. Mater. Sci.* **6**, 15-50 (1996).
41. Perdew, J. P. and Zunger, A. Self-interaction correction to density-functional approximations for many-electron systems. *Phys. Rev. B* **23**, 5048 (1981).
42. Perdew, J. P., Burke, K., and Ernzerhof, M. Generalized gradient approximation made simple. *Phys. Rev. Lett.* **77**, 3865 (1996).
43. Klimeš, J., Bowler, D. R., and Michaelides, A. Chemical accuracy for the van der Waals density functional. *J. Phys. Condens. Matter* **22**, 022201 (2010).

44. Klimeš, J., Bowler, D. R., and Michaelides, A. Van der Waals density functionals applied to solids. *Phys. Rev. B* **83**, 195131 (2011).
45. Dion, M. *et al.* Van der Waals density functional for general geometries. *Phys. Rev. Lett.* **92**, 246401 (2004).
46. Dudarev, S. L. *et al.* Electron-energy-loss spectra and the structural stability of nickel oxide: An LSDA+U study. *Phys. Rev. B* **57**, 1505 (1998).

**Acknowledgements:** This work was supported by the Center for Integrated Quantum Materials under NSF Grant DMR-1231319 (D.R.K., E.K., and S.F.), the DOE Office of Science, Basic Energy Sciences under award DE-SC0018935 (D.M.), as well as the Gordon and Betty Moore Foundation's EPiQS Initiative through grant GBMF4541 to P.J.-H. D.R.K. acknowledges partial support by the NSF Graduate Research Fellowship Program under Grant No. 1122374. R.C. acknowledges support from the Alfred P. Sloan Foundation. X.S. is supported by the Xu Xin International Student Exchange Scholarship from Nanjing University. E.K. and S.F. are also supported by the ARO MURI Award No. W911NF-14-0247. Work done at Ames Laboratory (M.X., R.A.R., and P.C.) was performed under Contract No. DE-AC02-07CH11358. R.A.R. was supported by the Gordon and Betty Moore Foundation's EPiQS Initiative through Grant GBMF4411. The computations in this paper were run on the Odyssey cluster supported by the FAS Division of Science, Research Computing Group at Harvard University.

**Author Contributions:** D.R.K., D.M., and P.J.-H. conceived the project. D.R.K. and D.M. grew the bulk $CrCl_3$ crystals, fabricated and measured the transport devices, and analyzed the data. Q.S. carried out Raman measurements under supervision of R.C. D.T.L. and S.F. carried out symmetry analysis and DFT calculations under supervision of E.K. M.X., R.A.R., and P.C. supplied the boron nitride crystals. All authors contributed to writing the manuscript.

**Competing Financial Interests:** The authors declare no competing financial interests.

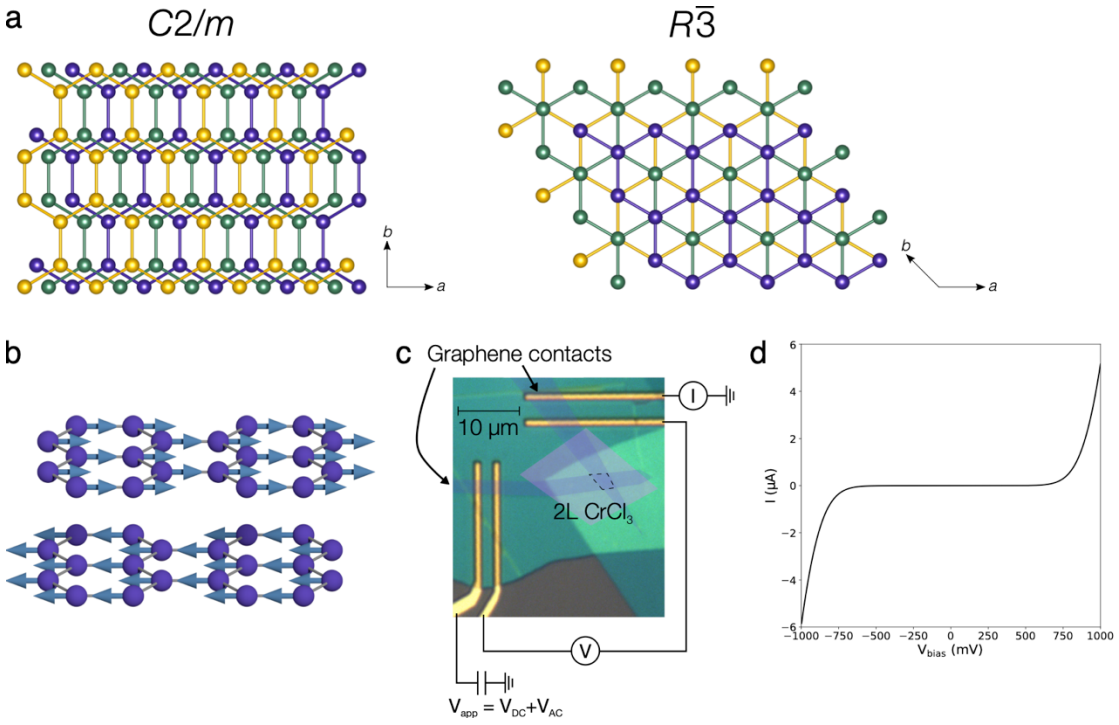


**Figure 1 | $CrCl_3$ stacking order and device characteristics. (a)** Stacking sequence of the Cr honeycomb sublattice in the *C*2/*m* (high temperature, left) and $R\bar{3}$ (low temperature, right) phases of $CrCl_3$ viewed perpendicular to the *ab*-plane. In both cases, the first and fourth layers are approximately aligned. **(b)** Schematic of moments in two adjacent layers at equilibrium. The moments lie in the *ab* plane. **(c)** False-color optical microscope image of a bilayer $CrCl_3$ tunnel junction device with four-point contact geometry for differential conductance measurements. **(d)** Current versus bias voltage for a trilayer tunnel junction at 4.2 K. The current was obtained by integration of the differential conductance with an AC bias voltage excitation of 50 mV.

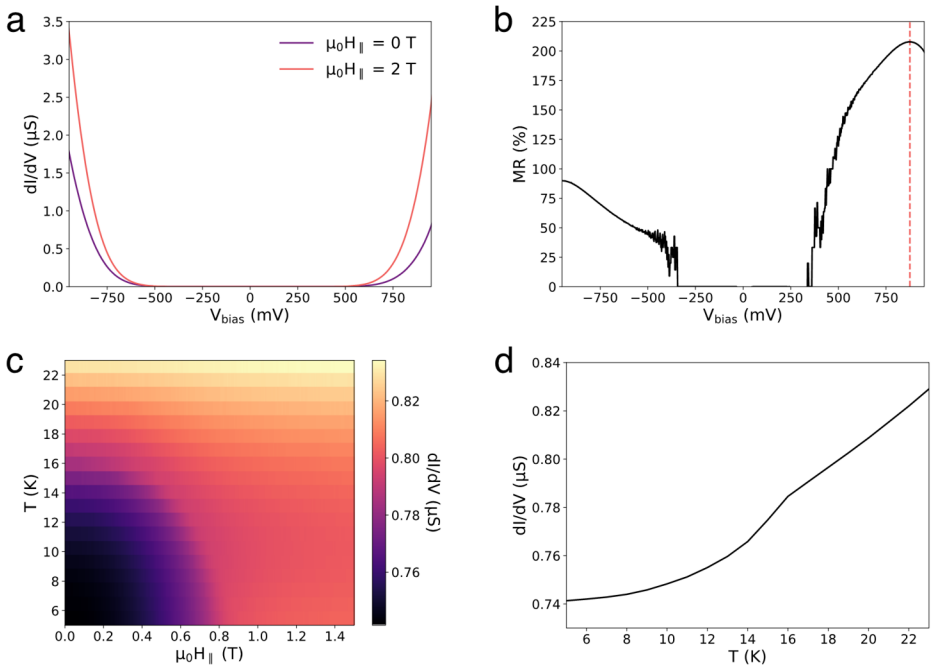


**Figure 2 | Magnetoresistance in $CrCl_3$ magnetic tunnel junctions. (a)** Differential conductance versus bias voltage for a tetralayer tunnel junction with an AC excitation of 50 mV at 300 mK. The data are taken at zero applied field (pink) and with an in-plane magnetic field of 2 Tesla (purple). **(b)** Magnetoresistance percent versus applied bias voltage for a tetralayer tunnel junction with a high-field in-plane magnetic field of 2 Tesla, extracted from **(a)**. The dashed line at a bias of 875 mV indicates the optimum bias for magnetoresistance. **(c)** Differential conductance versus applied in-plane magnetic field and temperature for a bilayer tunnel junction. The DC bias is -625 mV and the AC excitation is 50 mV. **(d)** Vertical line cut from **(c)** at zero applied magnetic field. The kink between 15 K and 16 K indicates $T_N$.

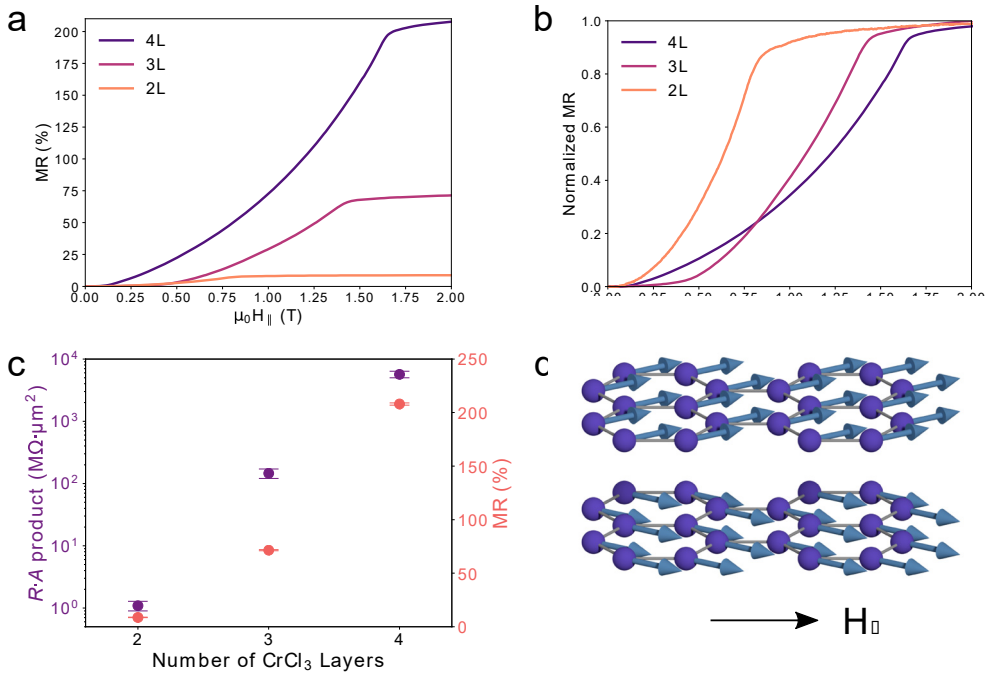


**Figure 3 | Thickness dependence of $CrCl_3$ magnetic tunnel junctions. (a)** Magnetoresistance versus applied in-plane magnetic field for bilayer, trilayer, and tetralayer tunnel junctions at finite applied bias and an AC excitation of 50 mV at 4 K. **(b)** Normalized magnetoresistance versus applied in-plane magnetic field. **(c)** Differential resistance-area product (purple) and magnetoresistance (pink) versus $CrCl_3$ layer number. The differential resistance was measured with an applied DC bias of 500 mV at 4 K for each device. Error bars in the differential resistance-area product and magnetoresistance represent estimated standard deviations arising from calculation of junction areas from optical microscope images and estimation of magnetoresistance plateaus, respectively. **(d)** Schematic of moments in two layers canting towards the in-plane applied field.

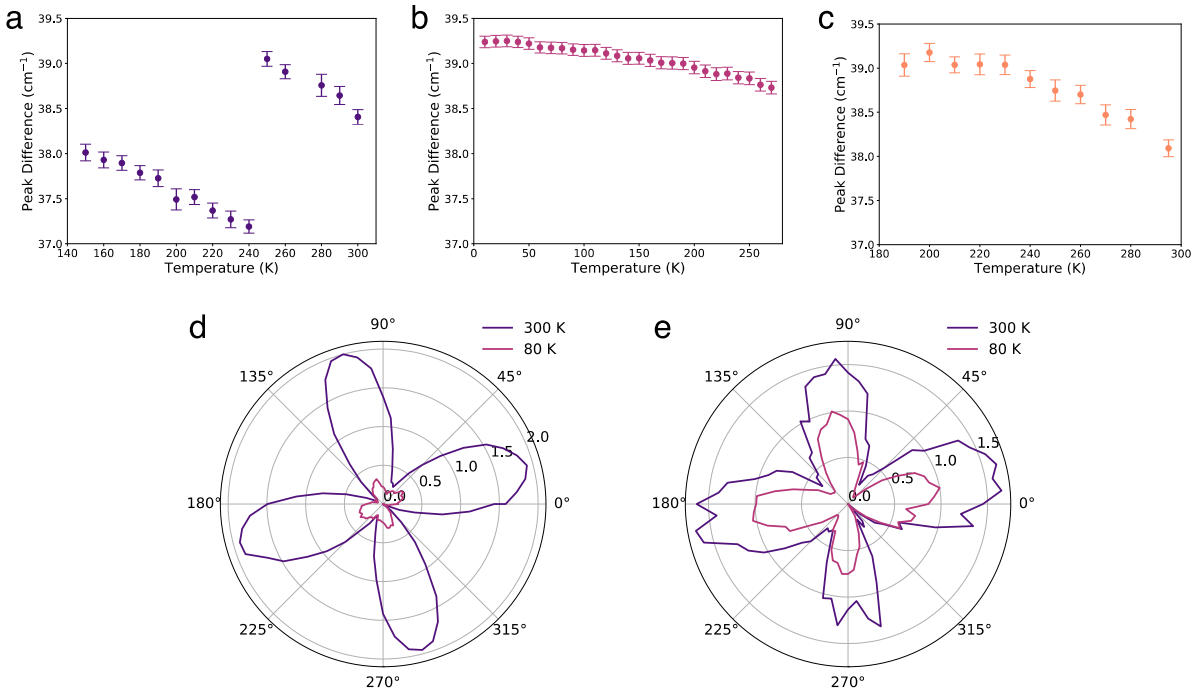


**Figure 4 | Raman spectroscopy of bulk and exfoliated $CrCl_3$. (a)** Difference between Raman peak positions of the 247 cm$^{-1}$ and 209 cm$^{-1}$ modes versus temperature for a bulk crystal of $CrCl_3$. A jump in the peak difference occurs around the crystallographic phase transition near 240 K. **(b)** The same peak difference versus temperature for an exfoliated 35 nm thick flake of $CrCl_3$ on a 90 nm $SiO_2$/Si substrate. The peak difference smoothly evolves down to 10 K without evidence of a phase transition. **(c)** The same peak difference versus temperature for an exfoliated 8 nm flake. **(d)** Peak position shift (in cm$^{-1}$) relative to minimum of 247 cm$^{-1}$ mode versus polarization angle for a bulk crystal. **(e)** Same as **(d)** for an exfoliated 17 nm thick flake on a 90 nm $SiO_2$/Si substrate. All error bars reflect a 2$\sigma$ confidence interval in fit parameters for the Raman peak positions.

## Methods:

### Bulk crystal growth

Bulk $CrCl_3$ crystals were grown by recrystallization of anhydrous $CrCl_3$ flakes. Approximately 1.0 g of the flakes (99.9%, Alfa Aesar) was loaded into a silica ampule in an inert environment and sealed under vacuum. The ampule was placed in a three-zone tube furnace with source, growth, and third zones held at 700ºC, 550ºC, and 625ºC, respectively, for a duration of 6 days. The source material was fully transported to the middle growth zone where it recrystallized into flat platelet crystals.

Hexagonal boron nitride (hBN) single crystals were grown from a high temperature, high pressure solution with an atomic Mg:B ratio of 1:0.7. A high pressure and high temperature Rockwell furnace was used to generate pressures up to 3.34 GPa and temperatures up to 1450°C. A 160 mg mass of $Mg_1B_{0.7}$ was put into a BN crucible, filling it to roughly 3/4 of its volume; the rest of crucible space was filled with BN powder. The crucible and a graphite heater were then placed in the middle of a pyrophyllite cube which was used as pressure medium for the high pressure furnace. The assembled cube is placed into the Rockwell furnace and pressure was applied at room temperature. After that the growth was (i) heated up to 1450°C over two hours, (ii) held at 1450°C for 1 hour, (iii) cooled down to 650°C over 6 hours, and (iv) cooled down to room temperature over 1 hour. Once cooled, the pressure was released. The pyrophyllite cube was then broken open and the BN crucible was removed and sealed in an evacuated amorphous silica tube for distillation of the excess Mg away from the hBN crystals. Distillation takes place over 3 hours, with one end of the sealed tube being held at 750°C and the other end hanging out of a clam furnace, around 100 – 200°C. After the distillation, the hBN crystals were mechanically separated from the BN crucible and $MgB_2$ single crystals.

### Device assembly

Exfoliation of few-layer flakes from the bulk $CrCl_3$ was carried out in an argon glove box to prevent hydration of the crystals. Optical contrast was employed to determine the thickness of each flake. The van der Waals magnetic tunnel junctions were then assembled by the dry transfer process in an argon environment.

The magnetic tunnel junctions were assembled by sequentially picking up flakes of boron nitride, few-layer graphite, $CrCl_3$, few-layer graphite, and boron nitride. The stacks were aligned such that the only vertical overlap between the two graphite electrodes is through the $CrCl_3$ tunnel barrier two to four layers in thickness. The use of top and bottom hexagonal boron nitride flakes provides protection from ambient conditions and an atomically flat substrate free of dangling bonds.

In each device, the final stack was transferred onto a silicon substrate wirebonded to a chip carrier with a 285 nm oxide layer also containing prepatterned Ti/Pd wires. The stack was aligned so that the two few-layer graphite electrodes contact the Ti/Pd wires.

## Transport measurements

Magneto-transport measurements were carried out in a helium-3 cryostat with an external magnetic field applied either parallel or perpendicular to the device. Differential conductance measurements were obtained using low frequency lock-in methods (excitation frequency < 20 Hz). Our DC measurements were performed by applying a DC bias to the sample and reading out the DC current through a current preamplifier. All measurements were performed at fixed temperature (300 mK or 4.2 K), with the exception of the temperature-dependent data shown in Fig. 2c and 2d.

## Raman measurements

Polarized Raman experiments were performed in a backscattering geometry using a confocal microscope spectrometer (Horiba Evolution) with a 50x objective lens and 532 nm laser with a power of 2.0 mW. The spectrometer integration times were 5 minutes and 30 minutes for bulk and exfoliated crystals, respectively. Each scan was taken twice and then averaged before analysis.

The incident laser beam was linearly polarized in the vertical direction and a half-wave plate was placed just before the objective. The analyzer was placed in front of the spectrometer entrance and kept vertical for parallel configuration (XX). For polarization dependence, the half-wave plate was rotated at a step of 2.5º from 0º to 180º.

## DFT calculations

Spin-polarized density functional theory (DFT) calculations were performed using PAW pseudopotentials[38] as implemented in the Vienna Ab initio Simulation Package (VASP)[39,40]. The energy cutoff for the plane wave basis was set at 350 eV with a 17x17x1 Γ-centered *k*-point grid. The Cl pseudopotential had 7 valence electrons ($3s^2 3p^5$) and Cr pseudopotentials with either 6 or 12 valence electrons were used ($3d^5 4s^1$ or $3p^6 3d^5 4s^1$, respectively). We used several exchange-correlation functionals: LDA[41], PBE[42], and optB86b-vdW exchange functional[43,44] with the vdW correlation functional[45]. Some calculations were performed using the LSDA+U method[46] with Hubbard U = 3 eV[27].

**Data Availability**: The data that support the findings of this study are available at the following URL: https://dataverse.harvard.edu/dataverse/crcl3